Earth, Planets and Space

FULL PAPER

Open Access

EUV signals associated with O^+ ions observed from ISS-IMAP/EUVI in the nightside ionosphere

Shin'ya Nakano[1,2*], Yuta Hozumi[3,4], Akinori Saito[5], Ichiro Yoshikawa[6], Atsushi Yamazaki[7], Kazuo Yoshioka[6] and Go Murakami[7]

Abstract

The extreme ultraviolet (EUV) imager, EUVI-B, on board the International Space Station (ISS) under the International Space Station–ionosphere-mesosphere-atmosphere plasmasphere cameras (ISS-IMAP) mission was originally intended to observe EUV emissions at 83.4 nm scattered by O^+ ions. During the mission, EUVI-B occasionally detected evident EUV signals in the umbra of the Earth. However, the source of the signals has not been verified. To evaluate the effect of the 83.4 nm EUV, we conduct a Monte Carlo simulation which considers multiple scattering of the 83.4 nm EUV by O^+ ions. In addition, we modeled the contribution of the 91.1 nm emission, which is due to recombination of O^+ ions and electrons, because the 91.1 nm EUV might affect the measurement from EUVI-B due to the wavelength range covered. The results suggest that the effect of the 83.4 nm EUV is likely to be negligible while the 91.1 nm EUV explains the observations from EUVI-B morphologically and quantitatively. We therefore conclude that the EUV signals observed by EUVI-B in the umbra of the Earth can largely be attributed to 91.1 nm emission due to recombination. This conclusion would facilitate the use of the EUVI-B data for reconstructing the O^+ density.

Keywords: O^+ ion, Ionosphere, Extreme ultraviolet measurement

Introduction

Ultraviolet imaging observation is a useful tool for diagnosing the state of the ionosphere. In particular, measurements of emissions associated with O^+ ions, which are the dominant species in the lower ionosphere, provide valuable information on spatio-temporal variations of the ionosphere. The most prominent emission from O^+ is the 83.4 extreme ultraviolet (EUV) emission (e.g., Meier 1991) and several observations of this emission have been conducted (e.g., McCoy et al. 1985; Stephan et al. 2019). The observations of airglow at 91.1 nm and 135.6 nm are used for investigating O^+ distributions, especially on the nightside (e.g., Dymond et al. 2004; Sagawa et al. 2005; Immel et al. 2006; Dymond et al. 2017c; Eastes et al. 2019).

The International Space Station–ionosphere-mesosphere-atmosphere Plasmasphere cameras (ISS-IMAP) mission operated two kinds of imagers on board the International Space Station (ISS). One was the Visible and near-Infrared Spectral Imager (VISI) (Sakanoi et al. 2011) and the other was the Extreme Ultraviolet Imagers (EUVI) (Yoshikawa et al. 2011). EUVI consisted of two telescopes, EUVI-A and EUVI-B. EUVI-A was designed to observe the 30.4 nm radiation from He^+ and EUVI-B was intended to observe the 83.4 nm radiation from O^+. As illustrated in Uji et al. (2014) and Hozumi et al. (2017), these two telescopes are directed toward the aft direction of the ISS orbit to conduct limb observations of the Earth's ionosphere. The EUVI telescopes thus acquired information on vertical and horizontal structures of the ionosphere and plasmasphere.

*Correspondence: shiny@ism.ac.jp
[1] The Institute of Statistical Mathematics, Tachikawa 190-8562, Japan
Full list of author information is available at the end of the article

The signals taken from EUVI-A were likely to be 30.4 nm EUV due to resonant scattering by He^+ ions (Hozumi et al. 2017). However, the source of the signals from EUVI-B has not been verified. Hozumi (2013) reported that EUVI-B sometimes detected evident EUV signals in the umbra of the Earth, though these nighttime signals were not satisfactorily explained. Indeed, modeling of the EUVI-B measurements is not easy. Since 83.4 nm EUV undergoes multiple scattering by O^+ ions in the ionosphere (e.g., Stephan , 2016; Geddes et al. , 2016), the relation with the O^+ density profile along the line of sight would be complicated. In addition, it should be noted that the wavelength range covered by EUVI-B was not narrow enough. Since EUVI-B covered the wavelength range from about 70 nm to 110 nm (Yoshikawa et al. 2011; Uji et al. 2014), it did not exclude the contribution of other nightglow emissions, such as the 91.1 nm, 98.9 nm, and 102.6 nm emissions. In particular, since the 91.1 nm emission due to recombination between O^+ ions and electrons is one of the prominent emissions on the nightside (Chakrabarti et al. 1984; Meier 1991; Feldman et al. , 1992), it is necessary to take into account its contribution.

The purpose of this paper is to clarify the source of the signals observed by EUVI-B to facilitate the use of the EUVI-B data. Since the EUVI-A and EUVI-B telescopes were operated when the ISS orbited in the umbra of the Earth (Uji et al. 2014), the EUV flux observed on the nightside is discussed. We conduct a Monte Carlo simulation to examine the effect of multiple scattering of the 83.4 nm EUV. We also examine the effect of the 91.1 nm EUV. The contribution of each effect is then quantitatively evaluated.

Observation

The operation of ISS-IMAP started in October 2012. The altitude of the ISS is about 400 km and the orbital inclination is 51°. The ISS-IMAP telescopes thus conducted imaging observations of the ionosphere at mid and low latitudes. The field of view of the imager EUVI-B was 13.2° × 13.2°. Figure 1 shows the EUV images taken from EUVI-B during 21:08:26–21:09:25 UT and 21:18:38–21:19:37 UT on December 26, 2012. In each panel, the orange contours indicate the altitude at the tangential point of the line of sight for each pixel. The altitudes from about 100–400 km were covered by the field of view of this imager. Each pixel shows the count of photons. The expected count C for $4\pi I$ Rayleighs of EUV flux was

$$C = \int 4\pi I(t) S\, dt \simeq 4\pi IST, \tag{1}$$

where S is the total sensitivity and T is the exposure time. S was equal to 0.0019 [counts/s/Rayleigh/bin] for EUVI-B at 83.4 nm (Uji et al. 2014). The exposure time T was

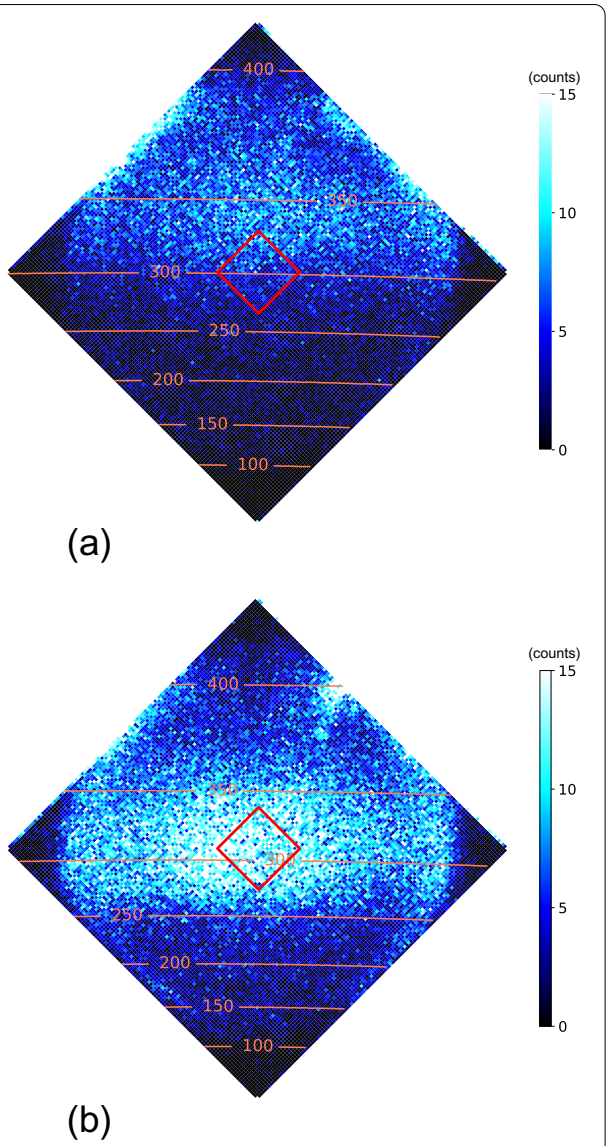

Fig. 1 EUV image taken from EUVI-B during 21:08:26–21:09:25 UT (**a**) and 21:18:38–21:19:37 UT (**b**) on December 26, 2012. The red square in each panel indicates the region where the EUV count is averaged to obtain Fig. 3. The orange contours in each panel indicate the altitude (in km) at the tangential point along the line of sight

60 s here. The expected count for 100 Rayleighs is thus about 11.4 for the 83.4 nm EUV. Figure 2 shows the position of the ISS from 21:02 UT to 21:25 UT on December 26, 2012. Since each telescope was directed toward the backward direction of the ISS orbit as described above, Fig. 1 captured the northward (equatorward) view from the ISS location. The ISS was located near the equator around 21:08 UT, and it was located at mid latitude in the southern hemisphere around 21:18 UT.

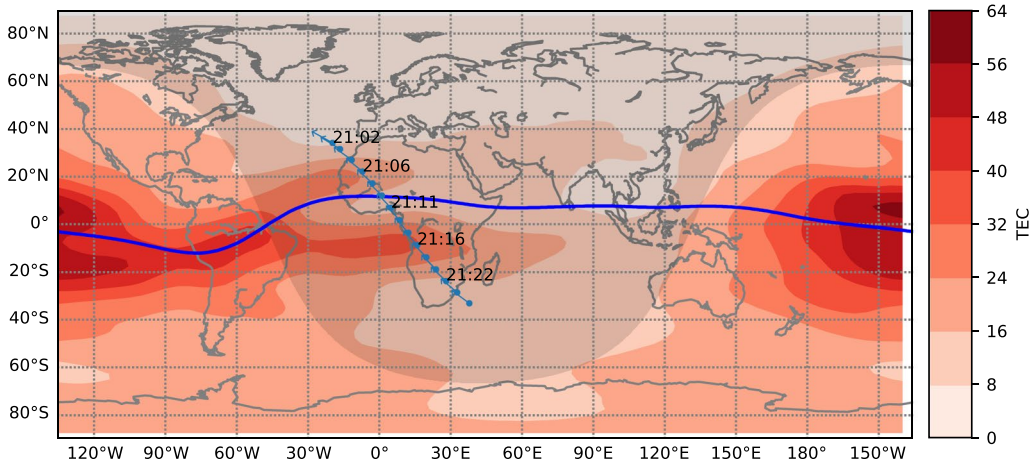

Fig. 2 Position of the ISS for the period from 21:02 UT to 21:25 UT on December 26, 2012. The tip of an arrow indicates the tangential point at each time. The blue solid line on the map indicates the dip equator. The TEC value is shown with the color contour

In Fig. 3, the blue line indicates the time profile of the EUV intensity from 21:02 UT to 21:25 UT on December 26, 2012, which corresponds to the period indicated in Fig. 2. The EUV intensity is shown by the averaged count over the 20×20 pixels surrounded by the red square in each panel of Fig. 1. The error bars in this figure shows the $\pm 2\sigma$ intervals where σ is the standard errors of the averaged count. Note that the observation was not necessarily taken every 60 s while the exposure time was 60 s. For reference, we plot the total electron content (TEC) value from IONEX (IOnosphere Map Exchange) at the ISS location with the orange line, and that at the tangential point of the line of sight with the green line. The averaged EUV count showed a bimodal profile, likely corresponding to the electron density structure indicated by the TEC observation. Figure 2 shows the position of the ISS for the corresponding period. The trough in the bimodal structure of the TEC was observed when the ISS crossed the dip equator, and thus it was regarded as the equatorial anomaly (e.g., Appleton 1946). The EUV observation thus corresponds well to the electron density structure. In the following, we work to reproduce this observational result.

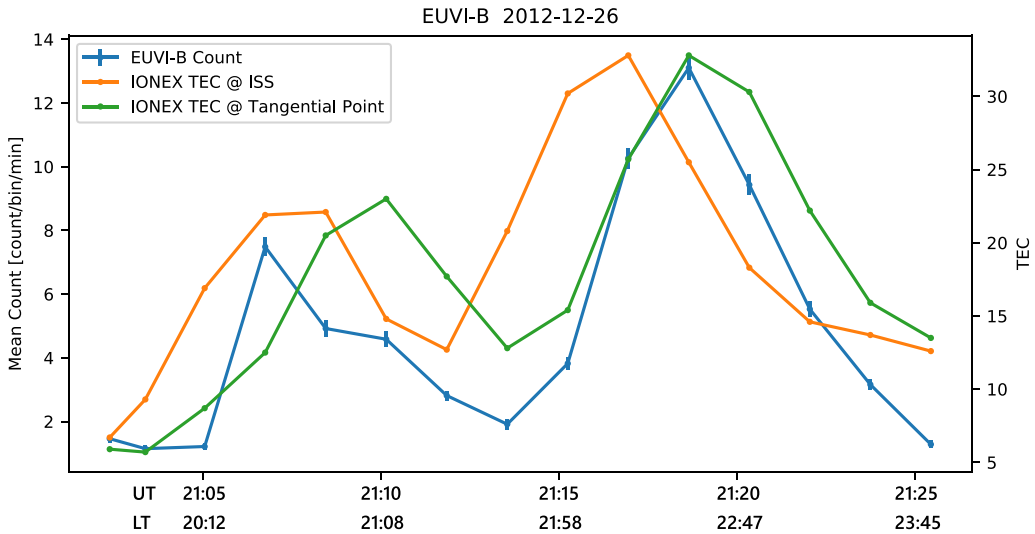

Fig. 3 Time profile of the averaged EUV count over the pixels surrounded by the red square in Fig. 1 (blue) during the period from 21:02 UT to 21:25 UT on December 26, 2012. The total electron content (TEC) value at the ISS location (orange) and that at the tangential point along the line of sight (green) are also plotted for reference. The horizontal axis indicates the universal time (UT) and the local time (LT) at the position of the ISS

Modeling of scattering

The EUV at 83.4 nm is attributed to resonant scattering by O^+ ions. The EUV flux due to the scattering, F_s[photons/($m^2 \cdot$ str $\cdot$ s)], is obtained by the following line-of-sight integral:

$$F_s = \int p(\nu') e^{-\tau(\nu',\ell)} \left[\frac{1}{4\pi} \int \bar{\sigma}_s(\nu) N(\boldsymbol{r}(\ell)) \Phi(\nu, \boldsymbol{r}(\ell), \omega)\, \mathrm{d}\omega\, \mathrm{d}\nu \right] \mathrm{d}\ell\, \mathrm{d}\nu', \tag{2}$$

where $\boldsymbol{r}$ denotes the location, ℓ is the distance of $\boldsymbol{r}$ from the observation site, $p(\nu')$ is the probability density function for the frequency of the scattered EUV ν', τ is the optical depth, $\bar{\sigma}_s$ is the scattering cross section, N is the O^+ number density, and Φ is the photon flux to be scattered. The photon flux is written as a function of the frequency ν, the location $\boldsymbol{r}$, and the direction ω. We hereinafter assume that the scattering is isotropic. We take the O^+ number density N from the International Reference Ionosphere (IRI) model (Bilitza et al. 2014). The optical depth τ is associated with absorption due to neutrals and it is given by combining the line-of-sight integral for each species:

$$\tau(\nu, \ell) = \int_0^\ell \bar{\sigma}_s(\nu) N(\boldsymbol{r}(s))\, \mathrm{d}s + \sum_i \int_0^\ell \alpha_i n_i(\boldsymbol{r}(s))\, \mathrm{d}s, \tag{3}$$

where i denotes absorbing species and α_i and n_i are the absorbing cross section and number density for each of the species, respectively. In this study, the absorption due to N_2, O, and O_2 is taken into account. The number densities for these absorbing species are given by the Naval Research Laboratory Mass Spectrometer and Incoherent Scatter Radar Exosphere (NRLMSISE-00) model (Picone et al. 2002), and the absorbing cross sections are taken to be 10.1×10^{-22} m^2, 3.9×10^{-22} m^2, and 10.4×10^{-22} m^2 for N_2, O, and O_2, respectively, according to Link et al. (1994). The probability density function of ν' is given as a Gaussian distribution:

$$p(\nu') = \frac{1}{\sqrt{2\pi\Delta_\nu^2}} \exp\left(-\frac{(\nu' - \nu_0)^2}{2\Delta_\nu^2} \right), \tag{4}$$

according to Eq. (14) in Appendix 1.

The scattering cross section $\bar{\sigma}_s$ should be dependent on the EUV frequency ν because of the thermal motion of the scattering O^+. We obtain the scattering cross section $\bar{\sigma}_s$ by the following equation

$$\bar{\sigma}_s(\nu) = \frac{e^2}{4\varepsilon_0 mc\sqrt{2\pi\Delta_\nu^2}} f_{12} \exp\left(-\frac{(\nu - \nu_0)^2}{2\Delta_\nu^2} \right), \tag{5}$$

as shown in Appendix1, where e is the elementary charge, ε_0 is the vacuum permittivity, m is the mass of a scattering ion (O^+), c is the light speed, f_{12} is the oscillator strength, ν_0 is the wave frequency at the center of the 83.4 nm resonance line, and Δ_ν is the scale of Doppler broadening given by Eq. (15). The oscillator strength is taken at $f_{12} = 0.122$ according to Meier (1991). In obtaining Δ_ν, the ion temperature is taken from the IRI model. The photon flux Φ in Eq. (2) depends on the direction ω. It is demanding to obtain Φ as a function of ω over the line of sight for computing Eq. (2). However, since we assume isotropic scattering, it is not necessary to resolve the dependence of the photon flux on the direction ω, and instead the number density of photons at $\boldsymbol{r}$ is sufficient to obtain F_s. Denoting the number density of photons (per volume and frequency) as ρ, Eq. (2) can be rewritten as

$$\begin{aligned} F_s &= \int p(\nu') e^{-\tau(\nu',\ell)} \left[\frac{1}{4\pi} \int \bar{\sigma}_s(\nu) N(\boldsymbol{r}(\ell)) c\rho(\nu, \boldsymbol{r}(\ell))\, \mathrm{d}\nu \right] \mathrm{d}\ell\, \mathrm{d}\nu' \\ &= \frac{c}{4\pi} \int p(\nu') e^{-\tau(\nu',\ell)} N(\boldsymbol{r}(\ell)) \left[\int \bar{\sigma}_s(\nu) \rho(\nu, \boldsymbol{r}(\ell))\, \mathrm{d}\nu \right] \mathrm{d}\ell\, \mathrm{d}\nu' \\ &= \frac{c}{4\pi} \int p(\nu') e^{-\tau(\nu',\ell)} N(\boldsymbol{r}(\ell)) A\, \mathrm{d}\ell\, \mathrm{d}\nu', \end{aligned} \tag{6}$$

where we denote

$$A = \int \bar{\sigma}_s(\nu) \rho(\nu, \boldsymbol{r}(\ell))\, \mathrm{d}\nu. \tag{7}$$

While the integral with $\mathrm{d}\ell$ and $\mathrm{d}\nu'$ was computed using the trapezoidal rule, we estimated the integral A by the Monte Carlo simulation in which the effect of multiple-scattering was considered. In this Monte Carlo simulation, we computed the propagation of a large number of photons from the EUV seeds on the sunlit ionosphere, and estimated the spatial distribution of the photon density resulting from the scattering by O^+ ions. The details of the Monte Carlo simulation are described in Appendix 2. As explained in the appendix, our Monte Carlo model would tend to overestimate the 83.4 nm flux for the target event on 26 December 2012 because of the choice of the parameter of the incident solar flux. The result of the Monte Carlo simulation would thus provide an upper-limit estimate of the 83.4 nm EUV flux.

Modeling of O^+ recombination

The EUV at 91.1 nm is emitted as a result of recombination of O^+ ions and electrons. The EUV flux due to the O^+ recombination is obtained by the following equation:

$$F_r = \frac{1}{4\pi} \int e^{-\tau(\ell)} \lambda n_e(\boldsymbol{r}(\ell))\, n_{O^+}(\boldsymbol{r}(\ell))\, d\ell \tag{8}$$

where n_e is the electron density and n_{O^+} is the O^+ ion density. The electron density n_e and the O^+ density n_{O^+} are taken from the IRI model; that is, we assume the same O^+ density distribution as for the 83.4 nm scattering model. The factor λ is the radiative recombination coefficient and $\lambda = 3.5 \times 10^{23} \times (1160/T)\,\mathrm{m}^3/\mathrm{s}$ (Meléndez-Alvira et al. 1999) where T is the electron temperature in Kelvin. The optical depth τ can be obtained according to Eq. (3). The absorbing species taken into account are N_2, O, and O_2. The absorption coefficients for 91.1 nm EUV are set to $14.5 \times 10^{-22}\,\mathrm{m}^2$, $3.93 \times 10^{-22}\,\mathrm{m}^2$, and $15.34 \times 10^{-22}\,\mathrm{m}^2$ for N_2, O, and O_2, respectively, according to Dymond et al. (2017c), which uses the values provided by Kirby et al. (1979) and Conway (1988). The number densities for the absorbing species are given according to the NRLMSISE-00 model.

Result

Figure 4 shows the model EUV time profile to be observed by EUVI-B for the 83.4 nm EUV as a result of resonant scattering (red line) and for the 91.1 nm EUV as a result of recombination (green line). In this figure, the expected count was obtained by the line-of-sight integral taken in the direction of the center of the square region over which the averaged EUV count was calculated in Fig. 3 (i.e., the region surrounded by the red square in each panel of Fig. 1). According to Fig. 3, we simulated the EUV measurement during the period 21:00–21:30 UT on December 26, 2012 with the expected count value for one minute which can be obtained with Eq. (1). The total sensitivity S was 0.0019 at 83.4 nm and 0.0018 at 91.1 nm. The simulation result indicated that the contribution of the 91.1 nm EUV dominated that of the 83.4 nm EUV during the period of interest when the ISS orbited on the nightside. In this figure, the mean count observed by EUVI-B, which was shown in Fig. 3, is overplotted (blue line). The expected count value for the simulated 91.1 nm EUV was quantitatively comparable to the observed averaged count although the simulated EUV intensity was a little weaker than the observed intensity for the second peak around 21:18 UT. On the other hand, the EUV intensity at 83.4 nm calculated with the Monte Carlo model was much less than the observed value. As explained in Appendix 2, our Monte Carlo simulation would gives an upper-limit estimate of the 83.4 nm EUV for this event. This result therefore suggests that the 83.4 nm EUV could not explain the observed EUV count in the umbra of the Earth. The simulation result for the 91.1 nm EUV also roughly reproduced the bimodal structure seen in the averaged count in Fig. 3. In contrast, Fig. 4 shows that the 83.4 nm EUV should only be discernable when the ISS orbited near the dusk. When the ISS crossed the equator, the 83.4 nm EUV was not detectable in this event because the ISS was located in the deep umbra. We therefore conclude that the observed signal from EUVI-B in Fig. 3 can be attributed to the 91.1 nm EUV. On the righthand side of Fig. 4, we show the scale in Rayleighs which is obtained by assuming that the observed signal is entirely due to the 91.1 nm EUV. The estimated photon flux values might contain systematic errors due to the uncertainty of the sensor sensitivity. However, since the sensor uncertainty cannot be quantified, the error bars in Fig. 4 just represents the $\pm 2\sigma$ intervals for the standard errors of the estimated flux.

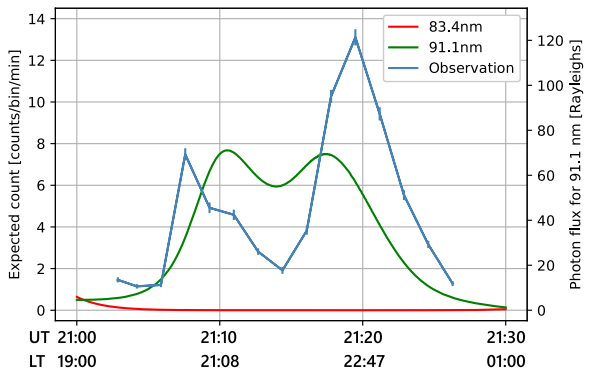

Fig. 4 Simulated EUV intensity for EUVI-B for 21:00–21:30 UT on December 26, 2012. The red line indicates the time profile for 83.4 nm EUV and the green line indicates the time profile for 91.1 nm EUV. The blue line shows the mean count observed by EUVI-B which was shown in Fig. 3 for comparison. The scale for converting the expected count into the photon flux in Rayleighs is also shown on the righthand side of this figure

Figure 5 shows the simulated images of the 91.1 nm EUV for EUVI-B at 21:08:56 UT and 21:19:08 UT on December 26, 2012. The color scale for each panel was adjusted in accord with Fig. 1. There are some discrepancies between Figs. 1 and 5. For example, while Fig. 1a suggests the source of the EUV emission shifted toward higher altitudes around 21:09 UT, the simulated emissions from the lower ionosphere were not as weak as the observed emissions. Figure 6 display the differences of the observed images in Fig. 1 from the simulated images in Fig. 5. The blue colors indicate that the observed EUV intensity exceeded the simulated intensity. Figure 6a suggests that the simulation underestimated the emissions from the lower altitudes. However, the EUV flux from the higher altitudes were well reproduced. Figure 6b suggests

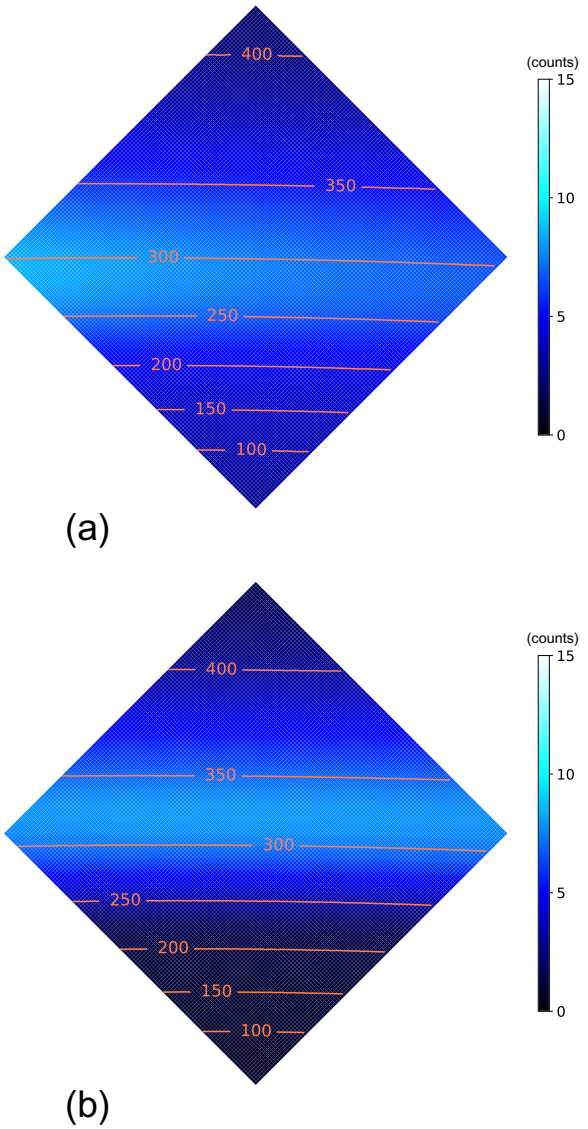

Fig. 5 Simulated images of 91.1 nm EUV for EUVI-B at 21:08:56 UT (**a**) and 21:19:08 UT (**b**) on December 26, 2012

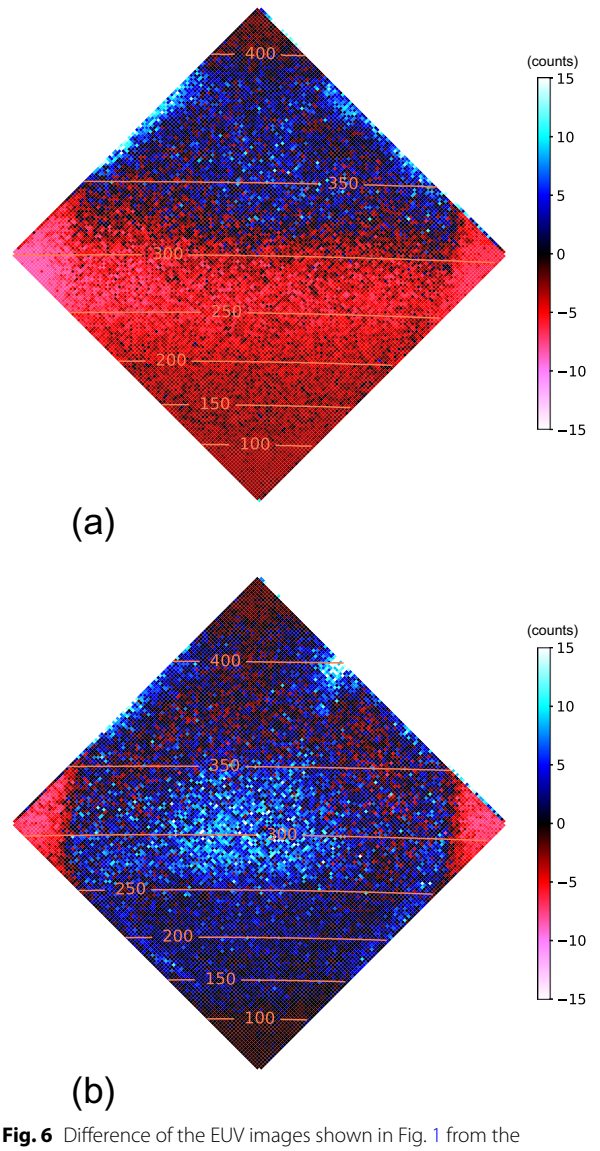

Fig. 6 Difference of the EUV images shown in Fig. 1 from the simulated images in Fig. 5 for the periods 21:08:26–21:09:25 UT (**a**) and 21:18:38–21:19:37 UT (**b**) on December 26, 2012

that the model underestimated the observed EUV signals around 21:19 UT as also suggested in Fig. 4. These discrepancies could be caused by variation of local conditions compared to the climatology represented in the models our simulation relied on. We determined the electron and O^+ densities by the IRI model. The densities of the absorbing neutrals were given by the NRLMSISE-00 model. Although these empirical models provide the average state for a given condition, they are not necessarily highly accurate for each particular event. In general, spatio-temporal variations tend to be smoothed in empirical models. That would be a reason why the dip of the EUV flux observed around 21:14 UT was less clear in the simulation result. Figure 7 compares the IONEX TEC values shown in Fig. 3 with the reconstructed TEC values derived from the IRI model. The IONEX TEC values at the ISS location and the tangential point are plotted with the thick orange and green lines, respectively. The IRI TEC values at the ISS location and the tangential point are plotted with the pale orange and green lines, respectively. There are visible differences between the IONEX TEC and the IRI TEC, which would introduce errors in our model. The trough in the bimodal structure is less clear in the IRI TEC. It should also be noted that the discrepancies might partly be caused by other nightglow

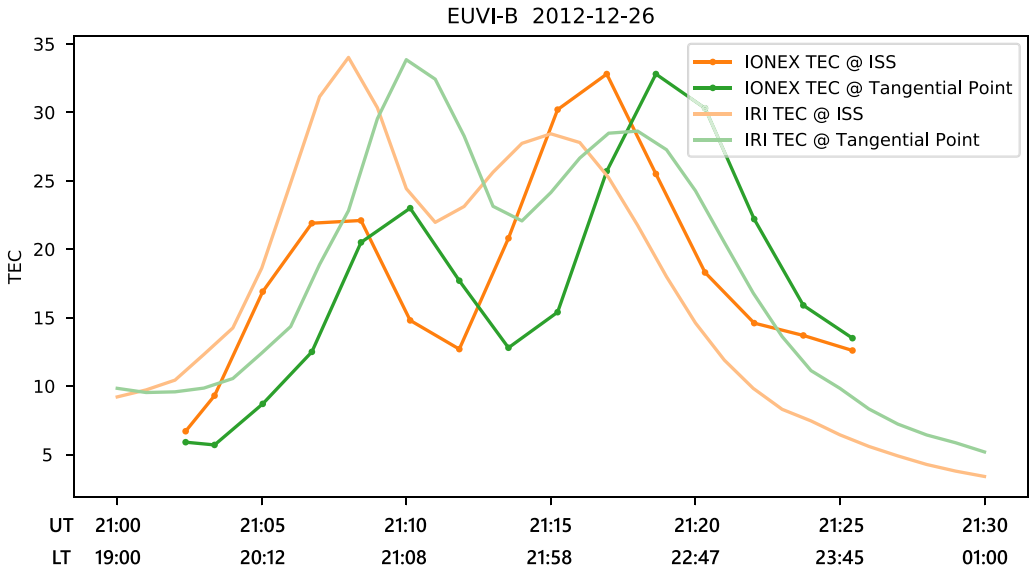

Fig. 7 Comparison of the IONEX TEC values shown in Fig. 3 with the TEC values reconstructed from the IRI model. The IONEX TEC values at the ISS location and the tangential point along the line of sight are plotted with the thick orange and green lines, respectively. The IRI TEC values at the ISS location and the tangential point are plotted with the pale orange and green lines, respectively

emissions. Considering the wavelength range covered by EUVI-B (70–110 nm), EUVI-B can also detect 98.9 nm and 102.6 nm emissions. The 98.9 nm and 102.6 nm emissions are typically weaker than the 83.4 nm emission by one order (Abreu et al. 1984; Chakrabarti et al. 1984; Meier 1991; Dymond et al. 2017b). Moreover, the sensitivity of EUVI-B was 0.0011 at 98.9 nm and 0.00047 at 102.6 nm, while it was 0.0018 at 91.1 nm. The contributions of the 98.9 nm and 102.6 nm EUV would therefore be too small to explain the entire difference. However, those emissions might, in part, contribute to the difference of the observation from the model prediction which assumes that the EUVI-B signals are totally attributed to the 91.1 nm EUV. At any rate, rough patterns in the observations were successfully reproduced by the simulation for the 91.1 nm EUV based on Eq. (8).

Discussion

As shown in the previous section, the EUV signals observed by EUVI-B in the umbra of the Earth can most likely be attributed to the 91.1 nm EUV. Although some discrepancies were seen in detailed structures between the simulated signals at 91.1 nm and the observed signals from EUVI-B, the observations were mostly reproduced by the model for the 91.1 nm EUV described in "Modeling of O^+ recombination" section. Figure 8 is a histogram of the observed photon flux to show how often EUV signals were observed by EUVI-B for each local time interval in nighttime. This histogram displays the frequency distribution of the photon flux, which was estimated by assuming that EUVI-B observed the 91.1 nm EUV, for the period from 21 December 2012 to 3 March 2013. In order to focus on low-latitude observations, the data taken when the ISS latitude was higher than 20° (20°N and 20°S) were excluded from this histogram. This figure shows that EUVI-B frequently observed EUV signals especially from 20:00 to 0:00 local time. This result is encouraging for the use of IMAP/EUVI-B data for studies of electron and O^+ density distributions in the ionosphere. Various efforts have been made to obtain the O^+ density distribution from remote optical measurements (e.g., Dymond et al. 1997; Qin et al. 2015). However, it is complicated to make an estimation from the 83.4 nm EUV data because of multiple scattering (e.g., Geddes

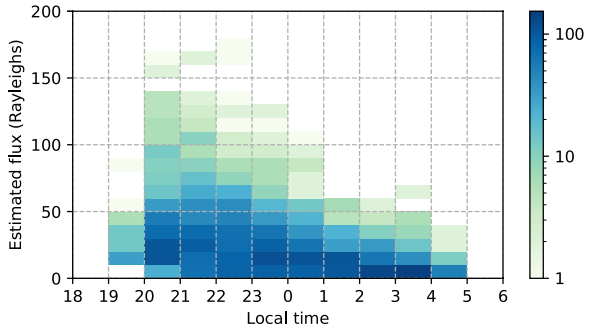

Fig. 8 Two-dimensional histogram of the estimated EUV flux when the ISS latitude was less than 20° for each local time interval in nighttime

et al. 2016). In contrast, estimating the O^+ density from the 91.1 nm EUV would be much easier because the relationship between the observed signals and the O^+ density is relatively simple. In the *F*-region, since the electron density is approximately equal to the O^+ density, Eq. (8) can be approximated as

$$F_r \approx \frac{1}{4\pi} \int e^{-\tau(\ell)} \lambda n_{O^+}^2 \, d\ell. \tag{9}$$

If the densities of the absorbing neutrals are known and thus the optical depth τ is known, only the O^+ density n_{O^+} is unknown. The problem for obtaining n_{O^+} thus becomes simple. Indeed, Dymond et al. (2017a, 2017c) demonstrated the reconstruction of the O^+ density distribution based on EUV data at 91.1 nm. Multiple images from different viewpoints according to the orbital motion can be used to estimate the three-dimensional ion distribution (e.g., Nakano et al. 2014). The EUVI-B data could thus be used to reconstruct the three-dimensional O^+ distribution in the vicinity of the ISS orbit.

When the EUVI-B signals are treated as the 91.1 nm EUV, the contribution of the 83.4 nm EUV should be regarded as noise. Although the simulation result in Fig. 4 suggested that the contribution of the 83.4 nm EUV was negligible for most of the period of interest, it would be meaningful to evaluate how deeply the 83.4 nm EUV penetrates the umbra of the Earth. We computed the omnidirectional flux of the 83.4 nm EUV at an altitude of 400 km using the Monte Carlo model described in "Modeling of scattering" section, where the omnidirectional flux is the flux averaged over 4π steradian. Figure 9 shows the estimated omnidirectional flux in Rayleighs for the nightside. The sunlit region at 400 km altitude was masked in this figure to highlight the penetration into the umbra. Since the EUV flux on the nightside would not be isotropic, the omnidirectional flux would not match the EUV flux observed by an imager. Figure 9, however, would provide a rough estimate of the contribution of the 83.4 nm EUV. The estimated omnidirectional flux could be discerned only near the terminator, and even there it was less than 1 Rayleigh. Therefore, it would be reasonable to assume the contribution of the 83.4 nm EUV to the EUVI-B measurements is negligible.

When using the EUVI-B data for estimating the O^+ density, we should take care of other factors which can affect the estimation. One issue is the uncertainty of the sensitivity value *S*. Although the uncertainty of S is unknown and it has not been quantified, it might introduce some bias to the estimate. We should also take into consideration the possible contributions of the 98.9 nm and 102.6 nm emissions. Although those emissions are inferred to be small as described above, their effects might cause some errors when estimating the O^+ density. However, these problems can be calibrated by comparing other independent ionospheric data such as the TEC data.

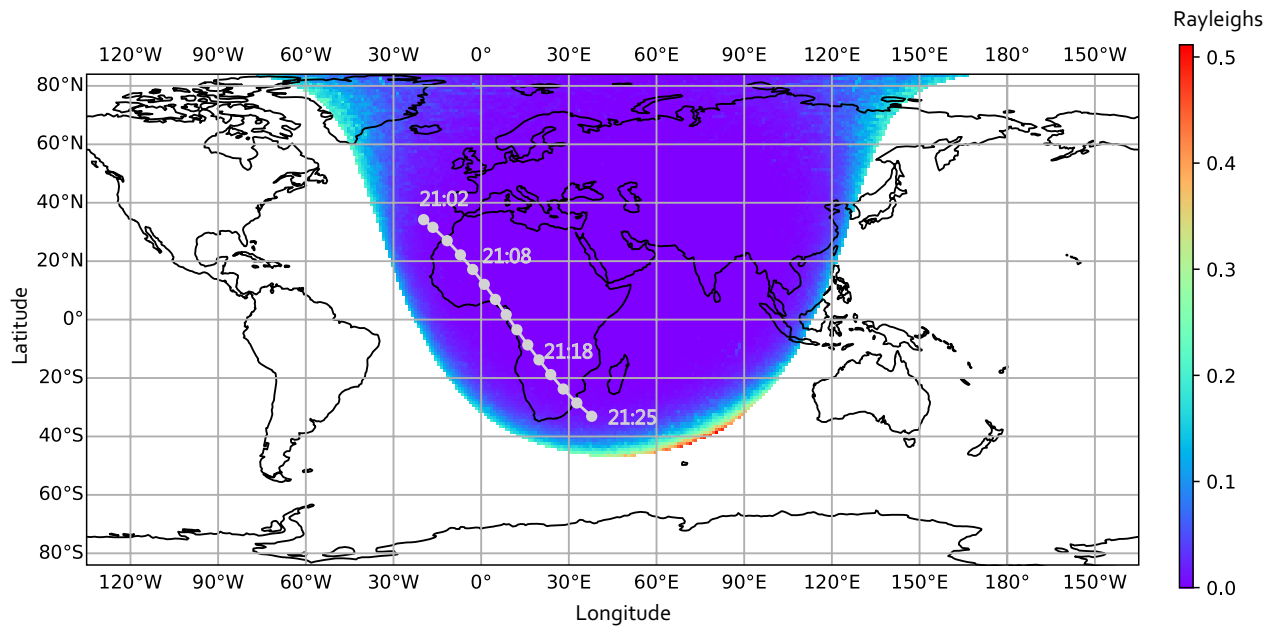

Fig. 9 Estimated omnidirectional flux of the 83.4 nm EUV at an altitude of 400 km on the nightside (in Rayleighs). The sunlit region at 400 km altitude is masked and only the flux in the umbra of the Earth is displayed

Summary

In order to explain the EUV signals observed from IMAP/EUVI-B on board the ISS on the nightside, we conducted two numerical modelings. One is a Monte Carlo simulation to examine the effect of the 83.4 nm emission due to the resonant scattering by O^+ ions. The other is a forward model to examine the effect of the 91.1 nm emission due to the recombination between electrons and O^+ ions. The simulation result suggests that the EUV signals observed from EUVI-B during nighttime were mainly the 91.1 nm EUV. The contribution of the 83.4 nm emission was typically negligible during nighttime. Since reconstructing the O^+ density distribution from the 91.1 nm EUV would be relatively easy, it is expected that the EUV signals observed from IMAP/EUVI-B will be useful for studies of electron and O^+ density distributions in the ionosphere.

Appendix 1. Scattering cross section

The scattering cross section $\bar{\sigma}_s$ is derived by considering the thermal motion of scattering ions. The scattering cross section of one O^+ particle for the EUV at frequency ν is

$$\sigma_{\rm p}(\nu,\nu_{\rm p}) = \frac{e^2}{4\varepsilon_0 mc} f_{12} L(\nu,\nu_{\rm p}) \tag{10}$$

(Meier 1991), where $\nu_{\rm p}$ is the center of resonance frequency in the observer's frame, ε_0 is the vacuum permittivity, e is the elementary charge, m is the mass of a scattering ion (O^+), c is the light speed, and f_{12} is the oscillator strength. The function L is given by

$$L(\nu,\nu_{\rm p}) = \frac{\gamma}{\pi[(\nu-\nu_{\rm p})^2+\gamma^2]}, \tag{11}$$

which is the probability density function of the Lorentz distribution, where the parameter γ determines the scale of the width of the distribution. The center of resonance frequency ν_p is perturbed by thermal motion of the scattering O^+ ion, and can be written as

$$\nu_{\rm p} = \left(1+\frac{\boldsymbol{n}_I\cdot\boldsymbol{v}_{\rm th}}{c}\right)\nu_0 = \left(1+\frac{v_{{\rm th},I}}{c}\right)\nu_0, \tag{12}$$

where ν_0 is the frequency at the center of the resonance line, $\boldsymbol{n}_I$ is the unit vector in the incident direction, $\boldsymbol{v}_{\rm th}$ is the thermal velocity of the O^+ ion, and $v_{{\rm th},I} = \boldsymbol{n}_I\cdot\boldsymbol{v}_{\rm th}$. Assuming that the O^+ ions follows an isotropic Maxwell distribution, the probability density function of $v_{{\rm th},i}$ can be written as follows:

$$p_{\rm v}(v_{{\rm th},i}) = \sqrt{\frac{m}{2\pi\kappa T}}\exp\left(-\frac{mv_{{\rm th},i}^2}{2\kappa T}\right), \tag{13}$$

where κ denotes the Boltzmann constant and T is the O^+ ion temperature. The probability density function of ν_p thus becomes

$$p(\nu_{\rm p}) = \frac{1}{\sqrt{2\pi\,\Delta_\nu^2}}\exp\left(-\frac{(\nu_{\rm p}-\nu_0)^2}{2\Delta_\nu^2}\right), \tag{14}$$

where Δ_ν is the scale of Doppler broadening given by

$$\Delta_\nu = \frac{\nu_0}{c}\sqrt{\frac{\kappa T}{m}}. \tag{15}$$

Integrating Eq. (10) over the distribution in Eq. (14), the cross section becomes

$$\bar{\sigma}_s(\nu) = \frac{e^2}{4\varepsilon_0 mc\sqrt{2\pi\,\Delta_\nu^2}} f_{12}\int \frac{\gamma}{\pi[(\nu-\nu_{\rm p})^2+\gamma^2]} \exp\left(-\frac{(\nu_{\rm p}-\nu_0)^2}{2\Delta_\nu^2}\right){\rm d}\nu_p. \tag{16}$$

Denoting $x_{\rm p} = (\nu_{\rm p}-\nu_0)/\Delta_\nu$ and $x = (\nu-\nu_0)/\Delta_\nu$, Eq. (16) can be rewritten as

$$\bar{\sigma}_s(x) = \frac{e^2}{4\varepsilon_0 mc\sqrt{2\pi\,\Delta_\nu^2}} f_{12}\int \frac{\gamma/\Delta_\nu}{\pi[(x_{\rm p}-x)^2+(\gamma/\Delta_\nu)^2]} \exp\left(-\frac{x_{\rm p}^2}{2}\right){\rm d}x_{\rm p}. \tag{17}$$

Since $\gamma \ll \Delta_\nu$ for the 83.4 nm EUV in the ionosphere (e.g., Meier 1991), we can adopt the following approximation:

$$\frac{\gamma/\Delta_\nu}{\pi[(x_{\rm p}-x)^2+(\gamma/\Delta_\nu)^2]} \approx \delta(x_{\rm p}-x) \tag{18}$$

to compute the integral in Eq. (17), where δ denotes the Dirac delta function, and Eq. (17) becomes

$$\begin{aligned}\bar{\sigma}_s(x) &= \frac{e^2}{4\varepsilon_0 mc\sqrt{2\pi\,\Delta_\nu^2}} f_{12}\int \delta(x_{\rm p}-x)\exp\left(-\frac{x_{\rm p}^2}{2}\right){\rm d}x_{\rm p} \\ &= \frac{e^2}{4\varepsilon_0 mc\sqrt{2\pi\,\Delta_\nu^2}} f_{12}\exp\left(-\frac{x^2}{2}\right).\end{aligned} \tag{19}$$

Therefore, the cross section averaged over the thermal motion of O^+ ions is obtained as follows:

$$\bar{\sigma}_s(\nu) = \frac{e^2}{4\varepsilon_0 mc\sqrt{2\pi\Delta_\nu^2}} f_{12} \exp\left(-\frac{(\nu-\nu_0)^2}{2\Delta_\nu^2}\right). \quad (20)$$

Appendix 2. Monte Carlo model for evaluating EUV scattering

We fix the step size $\Delta\ell$ for computing the photon propagation at $0.001R_E$ in this study where R_E is the Earth radius. Given the position of the photon j at the k-th step as $\boldsymbol{r}_{j,k}$, the transport of the photon in one step can be written as

$$\boldsymbol{r}_{j,k+1} = \boldsymbol{r}_{j,k} + \Delta\ell \boldsymbol{d}_{j,k} \quad (21)$$

if the photon is not scattered during this step, where $\boldsymbol{d}_{j,k}$ is the unit vector in the direction of the photon propagation. The probability that one photon is scattered during a transit over a small segment $d\ell$ is

$$dP_s(\nu) = \bar{\sigma}_s(\nu) N \mathrm{d}\ell, \quad (22)$$

and hence the length of the path over which the photon does not encounter a scattering event, s, obeys the following exponential distribution:

$$p(s) = \lambda \exp[-\lambda s], \quad (23)$$

where $\lambda = \bar{\sigma}_s(\nu)N$. At each step, we draw a random number s_t from the distribution in Eq. (23). If $s_t \geq \Delta\ell$, we regard that the photon does not scatter during this step and the direction of the photon propagation is not changed:

$$\boldsymbol{d}_{j,k+1} = \boldsymbol{d}_{j,k}. \quad (24)$$

On the other hand, if $s_t < \Delta\ell$, the direction of the photon propagation is changed at

$$\boldsymbol{r}^*_{j,k} = \boldsymbol{r}_{j,k} + s_t \boldsymbol{d}_{j,k}, \quad (25)$$

and $\boldsymbol{r}_{j,k+1}$ becomes

$$\boldsymbol{r}_{j,k+1} = \boldsymbol{r}_{j,k} + s_t \boldsymbol{d}_{j,k} + (\Delta\ell - s_t)\boldsymbol{d}_{j,k+1}, \quad (26)$$

where $\boldsymbol{d}_{j,k+1}$ is a unit vector in a random direction, which is drawn from the uniform distribution on the unit sphere. As a result of the scattering, the wave frequency ν for the photon j changes according to the thermal motion of the scattering O^+. In this Monte Carlo model, if the direction of the photon propagation is changed, the wave frequency is also changed and the new frequency ν_{k+1} is assumed to obey the following probability distribution independent of the previous frequency as follows:

$$p(\nu_{k+1}|\nu_k) = p(\nu_{k+1}) = \frac{1}{\sqrt{2\pi\Delta_\nu^2}} \exp\left(-\frac{(\nu_{k+1}-\nu_0)^2}{2\Delta_\nu^2}\right). \quad (27)$$

according to Eq. (14). The computation of the photon propagation is continued until the photon escapes the simulation domain. The lower and upper boundaries of the simulation domain were taken to be 100 km and 3600 km in altitude. If the photon went out of the outer boundary, we assumed that it escaped toward the magnetosphere and we stopped the computation of its trajectory. If the photon dropped out of the inner boundary, we assumed that it was absorbed in the atmosphere and also stopped the computation.

If the sequence of photon positions is recorded at discrete steps $\{\boldsymbol{r}_{j,0}, \boldsymbol{r}_{j,1}, \boldsymbol{r}_{j,2}, \ldots\}$ for each test photon j, $(j = 1, \ldots, J)$, we can obtain a sample set of the photons flowing through the ionosphere by collecting the sequences of photon positions for all of the J test photons. ρ can be estimated from this sample set. We divide the simulation domain into bins of 1° (in longitude) $\times$ 0.5° (in latitude) $\times$ 10 km (in altitude), and the photon density for each bin is obtained as follows:

$$\hat{A}_m = \frac{1}{V_{B_m}} \sum_{\boldsymbol{r}_{j,k} \in B_m} w_{j,k} \bar{\sigma}_s(\nu_{j,k}), \quad (28)$$

where B_m denotes the m-th bin, V_{B_m} is the volume of the bin B_m, and $w_{j,k}$ is the weight of an individual photon sample at $\boldsymbol{r}_{j,k}$. $w_{j,k}$ represents the number of real photons represented by the j-th test photon. To consider the absorption due to neutrals, it is updated at each step according to the following equation:

$$w_{j,k+1} = w_{j,k} \exp(-\tau_{j,k}), \quad (29)$$

where the optical depth $\tau_{j,k}$ for one step is approximated as

$$\tau_{j,k} \approx \Delta\ell \sum_i \alpha_i n_i(\boldsymbol{r}_{j,k}). \quad (30)$$

The initial source of the EUV at 83.4 nm is mainly the photoionization of atomic oxygen due to solar EUV less than 43.6 nm (e.g., Stephan 2016). We draw the initial position of each test photon, $\boldsymbol{r}_{j,0}$, according to a uniform distribution over the sunlit simulation domain. However, the EUV emission due to the photoionization would not be uniform over the ionosphere because the atomic oxygen density is not uniform. We set the initial weight $w_{j,0}$ to represent the amount of initial EUV photons generated by the photoionization. We assume that the number

of initial photons generated due to the photoionization per volume per time can be written in the following form:

$$Q_0(\boldsymbol{r}) = \zeta n_{\mathrm{O}}(\boldsymbol{r}) \exp(-\tau_s) \tag{31}$$

where n_{O} is the atomic oxygen density, τ_s is the attenuation coefficient of the solar EUV radiation at $\boldsymbol{r}$, and ζ is a constant. τ_s is determined after considering the absorption of the incident solar EUV due to photoionization due to O. We assume $\tau_s = 0$ at the upper boundary of the simulation domain. We calculate τ_s below the upper boundary by integrating the absorption from the upper boundary to the point $\boldsymbol{r}_{j,0}$ where the absorption cross section is assumed to be $1.0 \times 10^{-21}\mathrm{m}^2$ in order to be comparable to the literature values, such as that of Kirby et al. (1979) and Meier et al. (2007). The initial weight $w_{j,0}$ is then set as follows:

$$w_{j,0} = \frac{V_{\mathrm{sunlit}}}{M V_{B(\boldsymbol{r}_{j,0})}} \frac{Q_0(\boldsymbol{r}_{j,0})}{c} \tag{32}$$

where V_{sunlit} is the volume of the sunlit region of the simulation domain, $V_{B(\boldsymbol{r}_{j,0})}$ is the volume of the bin which $\boldsymbol{r}_{j,0}$ belongs to, and M is the total number of test photons used in this Monte Carlo simulation. Since $(V_{B(\boldsymbol{r}_{j,0})}/V_{\mathrm{sunlit}})M$ is the expected number of initial photons in the bin $B(\boldsymbol{r}_{j,0})$, $w_{j,0}$ corresponds to the number of real photons represented by the j-th test photon. In our Monte Carlo simulation, the number of test photons M was set to be 14.4×10^{10}. The simulation took about 4 h by using a computer with 80 CPUS (Intel Xeon Gold 6154) each of which has 18 cores (1440 cores in total).

The parameter ζ should be determined according to the solar EUV irradiance and the photoionization cross section over the wavelength band which can contribute to the 83.4 nm emission. However, it is complicated to integrate the effect of EUV irradiance with various wavelengths. To avoid having to model the photoionization over a wide wavelength band, we tune the parameter ζ by comparing the simulation result with the dayside observations reported by Stephan (2016). The 83.4 nm EUV observation would include the initial source EUV due to the photoionization as well as the EUV after scattering by O^+ ions, especially on the dayside. Therefore, converting the photon flux into the unit of Rayleighs, the observed 83.4 nm EUV becomes

$$4\pi I_s = 10^{-6} 4\pi F_s + 10^{-6} \int Q_0(\boldsymbol{r})\, \mathrm{d}\ell. \tag{33}$$

Figure 10 shows the simulated altitudinal profile of the EUV photon flux for comparing the observation from the Defense Meteorological Satellite Program (DMSP) F19 satellite shown by Stephan (2016). We simulated the observation from 850 km altitude after calibrating the parameter ζ. The tangent point of the line of sight was set at 40° in latitude and 0722 LT on 6 September in accord with Fig. 1 in the paper by Stephan (2016). Since the DMSP observation showed that the EUV intensity peaked around 250 km in altitude and the peak intensity was about 650 Rayleighs, we adjusted ζ so that the peak intensity is similar to this DMSP observation. The incident solar flux on 26 December 2012 examined in this study must be different from that on 6 September 2014 examined by Stephan (2016). While the F10.7 flux was 110 on 26 December 2012, it 157 on 6 September 2014. This Monte Carlo model would thus tend to overestimate the 83.4 nm flux for the target event. However, we do not fix the difference in the solar flux between the two events because an upper-limit estimate of the 83.4 nm EUV flux is enough for the purpose of this study.

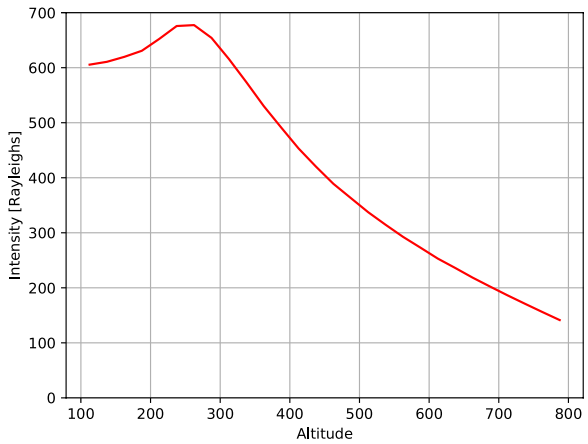

Fig. 10 Simulated altitudinal profile of the EUV photon flux (in Rayleighs) where the tangent point of the line of sight was set at 40° in latitude and 0722 LT on 6 September

Abbreviations

EUV: Extreme ultraviolet; ISS: International Space Station; ISS-IMAP: International Space Station–ionosphere-mesosphere-atmosphere Plasmasphere cameras; EUVI: Extreme Ultraviolet Imagers; TEC: total electron content; IONEX: IOnosphere Map Exchange; IRI: International Reference Ionosphere; NRLMSISE: Naval Research Laboratory Mass Spectrometer and Incoherent Scatter Radar Exosphere; DMSP: Defense Meteorological Satellite Program.

Acknowledgements

The Monte Carlo computation in this study was carried out on the Supercomputer System for Statistical Science at ISM under the ISM Cooperative Research Program (2020-ISMCRP-2003).

Authors' contributions

SN conducted the numerical modelings and simulation. YH and AS conceived the study and processed the ISS-IMAP/EUVI-B data. IY, AY, KY, and GM developed the ISS-IMAP/EUVI and calibrated the data. All authors read and approved the final manuscript.

Funding
The authors received no specific funding for this work.

Availability of data and materials
ISS-IMAP/EUVI data are available via e-mail inquiry to Akinori Saito at Kyoto University (saitoua@kugi.kyoto-u.ac.jp). The IONEX TEC data were obtained via "https://cddis.nasa.gov/archive/gnss/products/ionex/". The F10.7 solar radio flux data were obtained from "https://www.spaceweather.gc.ca/forecast-prevision/solar-solaire/solarflux/sx-en.php".

Declarations

Competing interests
The authors declare that they have no competing interests.

Author details
[1]The Institute of Statistical Mathematics, Tachikawa 190-8562, Japan. [2]Center for Data Assimilation Research and Applications, Joint Support Center for Data Science Research, Tachikawa 190-8562, Japan. [3]University of Electro-Communications, Chofu, Japan. [4]National Institute of Information and Communications Technology, Koganei, Japan. [5]Graduate School of Science, Kyoto University, Kyoto, Japan. [6]Graduate School of Frontier Sciences, The University of Tokyo, Kashiwa, Japan. [7]Institute of Space and Astronautical Science, Japan Aerospace Exploration Agency, Sagamihara, Japan.

Received: 27 March 2021 Accepted: 11 July 2021
Published online: 28 July 2021

References

Abreu VJ, Dalgarno A, Yee JH, Chakrabarti S, Solomon SC (1984) The OI 989-Å tropical nightglow. Geophys Res Lett 11:569–571
Appleton EV (1946) Two anomalies in the ionosphere. Nature 157:691
Bilitza D, Altadill D, Zhang Y, Mertens C, Truhlik V, Richards P, McKinnell L-A, Reinisch B (2014) The International Reference Ionosphere 2012—a model of international collaboration. J Space Wea Space Clim 4:A07. https://doi.org/10.1051/swsc/2014004
Chakrabarti S, Kimble R, Bowyer S (1984) Spectroscopy of the EUV (350–1400 Å) nightglow. J Geophys Res 89:5660–5664
Conway RR (1988) Photoabsorption and photoionization cross sections of O, O_2, and N_2 for photoelectron production calculations: a compilation of recent laboratory measurements, NRL Memorandum Report 6155. Washington D.C, Naval Research Laboratory
Dymond KF, Thonnard SE, McCoy RP, Thomas RJ (1997) An optical remote sensing technique for determining nighttime *F* region electron density. Radio Sci 32:1985–1996
Dymond KF, Budzien SA, Nicholas AC, Thonnard SE, McCoy RP, Thomas RJ, Huba JD, Joyce G (2004) Ionospheric response to the solar flare of 14 July 2000. Radio Sci 39. https://doi.org/10.1029/2002RS002842
Dymond KF, Budzien SA, Hei MA (2017a) Ionospheric-thermospheric UV tomography: 1. Image space reconstruction algorithm. Radio Sci 52:338–356. https://doi.org/10.1002/2015RS005869
Dymond KF, Nicholas AC, Budzien SA, Coker C, Stephan AW, Chua DH (2017b) The Special Sensor Ultraviolet Limb Imager instruments. J Geophys Res 122:2674–2685. https://doi.org/10.1002/2016JA022763
Dymond KF, Nicholas AC, Budzien SA, Stephan AW, Coker C, Hei MA, Groves KM (2017c) Ionospheric-thermospheric UV tomography: 2. Comparison with incoherent scatter radar measurements. Radio Sci 52:357–366. https://doi.org/10.1002/2015RS005873
Eastes RW, Solomon SC, Daniell RE, Anderson DN, Burns AG, England SL, Martinis CR, McClintock WE (2019) Global-scale observations of the equatorial ionization anomaly. Geophys Res Lett 46:9318–9326. https://doi.org/10.1029/2019GL084199
Feldman PD, Davidsen AF, Blair WP, Bowers CW, Durrance ST, Kriss GA, Ferguson HC, Kimble RA, Long KS (1992) The spectrum of the tropical oxygen nightglow observed at 3Å resolution with the Hopkins Ultraviolet Telescope. Geophys Res Lett 19:453–456
Geddes G, Douglas E, Finn SC, Cook T, Chakrabarti S (2016) Inverting OII 83.4 nm dayglow profiles using Markov chain radiative transfer. J Geophys Res 121:11249–11260. https://doi.org/10.1002/2016JA023168
Hozumi Y (2013) Imaging observation of plasma structures in the Earth's upper atmosphere from the International Space Station, Master's thesis. Kyoto Univ, Graduate School of Science
Hozumi Y, Saito A, Yoshikawa I, Yamazaki A, Murakami G, Yoshioka K, Chen C-H (2017) Global distribution of the He+ column density observed by Extreme Ultra Violet Imager on the International Space Station. J Geophys Res 122:7670–7682. https://doi.org/10.1002/2016JA023534
Immel TJ, Sagawa E, England SL, Henderson SB, Hagan ME, Mende SB, Frey HU, Swenson CM, Paxton LJ (2006) Control of equatorial ionospheric morphology by atmospheric tides. Geophys Res Lett 33:L15108. https://doi.org/10.1029/2006GL026161
Kirby K, Constantinides ER, Babeu S, Oppenheimer M, Victor GA (1979) Photoionization and photoabsorption cross sections of He, O, N_2 and O_2 for aeronomic calculations. Atom Data Nucl Data Tables 23:63–81
Link R, Evans JS, Gladstone GR (1994) The O^+ 834-Å dayglow: revised cross sections. J Geophys Res 99:2121–2130
McCoy RP, Anderson DE Jr, Chakrabarti S (1985) F_2 region ion densities from analysis of O^+ 834-Å airglow: a parametric study and comparisons with satellite data. J Geophys Res 90:12257–12264
Meier RR (1991) Ultraviolet spectroscopy and remote sensing of the upper atmosphere. Space Sci Rev 58:1–185
Meier RR, McLaughlin BM, Warren HP, Bishp J (2007) Atomic oxygen photoionization rates computed with high resolution cross sections and solar flaxes. Geophys Res Lett 34:L01104. https://doi.org/10.1029/2006GL028484
Meléndez-Alvira DJ, Meier RR, Picone JM, Feldman PD, McLaughlin BM (1999) Analysis of the oxygen nightglow measured by the Hopkins Ultraviolet Telescope: implications for ionospheric partial radiative recombination rate coefficients. J Geophys Res 104:14901–14913
Nakano S, Fok M-C, Brandt PC, Higuchi T (2014) Estimation of temporal evolution of the helium plasmasphere based on a sequence of IMAGE/EUV images. J Geophys Res 119:3708–3723. https://doi.org/10.1002/2013JA019734
Picone JM, Hedin AE, Drob DP, Aikin AC (2002) NRLMSISE-00 empirical model of the atmosphere: statistical comparisons and scientific issues. J Geophys Res 107(A12):1468. https://doi.org/10.1029/2002JA009430
Qin J, Makela JJ, Kamalabadi F, Meier RR (2015) Radiative transfer modeling of the OI 135.6 nm emission in the nighttime ionosphere. J Geophys Res 120:10116–10135. https://doi.org/10.1002/2015JA021687
Sagawa E, Immel TJ, Frey HU, Mende SB (2005) Longitudinal structure of the equatorial anomaly in the nighttime ionosphere observed by IMAGE/FUV. J Geophys Res 110:A11302. https://doi.org/10.1029/2004JA010848
Sakanoi T, Akiya Y, Yamazaki A, Otsuka Y, Saito A, Yoshikawa I (2011) Imaging observation of the Earth's mesosphere, thermosphere and ionosphere by VISI of ISS-IMAP on the International Space Station. IEEJ Trans. Fundam. Mater. 131:983–988. https://doi.org/10.1541/ieejfms.131.983
Stephan AW (2016) Advances in remote sensing of the daytime ionosphere with EUV airglow. J Geophys Res 121:9284–9292. https://doi.org/10.1002/2016JA022629
Stephan AW, Finn SC, Cook TA, Geddes G, Chakrabarti S, Budzien SA (2019) Imaging of the daytime ionospheric equatorial arcs with extreme and far ultraviolet airglow. J Geophys Res 124:6074–6086. https://doi.org/10.1029/2019JA026624
Uji K, Yoshikawa I, Yoshioka K, Murakami G, Yamazaki A (2014) Observations of the Earth's ionosphere and plasmasphere from International Space Station, Trans. JSASS Aerospace Tech. Japan, 12, Tn47–Tn50
Yoshikawa I, Homma T, Sakai K, Murakami G, Yoshioka K, Yamazaki A, Sakanoi T, Saito A (2011) Imaging observation of the Earth's plasmasphere and ionosphere by EUVI of ISS-IMAP on the International Space Station. IEEJ Trans. Fundam. Mater. 131:1006–1010. https://doi.org/10.1541/ieejfms.131.1006

Publisher's Note